JACS
JOURNAL OF THE AMERICAN CHEMICAL SOCIETY

Static Rashba Effect by Surface Reconstruction and Photon Recycling in the Dynamic Indirect Gap of $APbBr_3$ (A = Cs, CH_3NH_3) Single Crystals

Hongsun Ryu, Dae Young Park, Kyle M. McCall, Hye Ryung Byun, Yongjun Lee, Tae Jung Kim, Mun Seok Jeong, Jeongyong Kim, Mercouri G. Kanatzidis, and Joon I. Jang*

Cite This: https://dx.doi.org/10.1021/jacs.0c09132

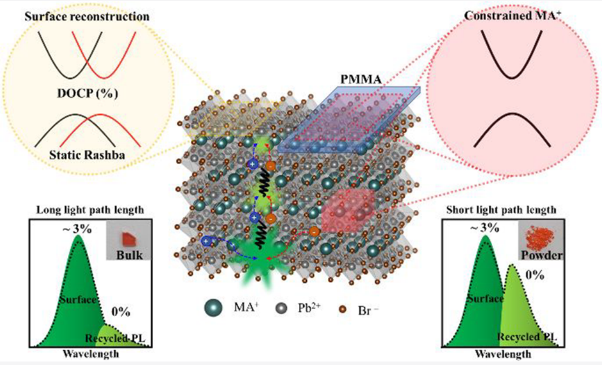

ABSTRACT: Recently, halide perovskites have gained significant attention from the perspective of efficient spintronics owing to the Rashba effect. This effect occurs as a consequence of strong spin−orbit coupling under a noncentrosymmetric environment, which can be dynamic and/or static. However, there exist intense debates on the origin of broken inversion symmetry since the halide perovskites typically crystallize into a centrosymmetric structure. In order to clarify the issue, we examine both dynamic and static effects in the all-inorganic $CsPbBr_3$ and organic−inorganic $CH_3NH_3PbBr_3$ ($MAPbBr_3$) perovskite single crystals by employing temperature- and polarization-dependent photoluminescence excitation spectroscopy. The perovskite single crystals manifest the dynamic effect by photon recycling in the indirect Rashba gap, causing dual peaks in the photoluminescence. However, the effect vanishes in $CsPbBr_3$ at low temperatures (<50 K) accompanied by a striking color change of the crystal, arising presumably from lower degrees of freedom for inversion symmetry breaking associated with the thermal motion of the spherical Cs cation compared with the polar MA cation in $MAPbBr_3$. We also show that the static Rashba effect occurs only in $MAPbBr_3$ below 90 K, presumably due to surface reconstruction via MA-cation ordering, which likely extends across a few layers from the crystal surface to the interior. We further demonstrate that this static Rashba effect can be completely suppressed upon surface treatment with polymethyl methacrylate (PMMA) coating. We believe that our results provide a rationale for the Rashba effects in halide perovskites.

■ INTRODUCTION

Halide perovskites have emerged as "miracle" materials for optoelectronic applications because of their superior optical, electronic, and structural properties such as high absorption coefficient,[1] defect tolerance,[2] band-gap tunability,[3−5] and easy preparation methods.[6−8] For instance, organic−inorganic halide perovskites (OIHPs) have been investigated in the form of thin films as highly efficient light harvesters as they have a long carrier lifetime and a long diffusion length.[6,9,10] On the other hand, all-inorganic halide perovskites (AIHPs) have been prepared into nanocrystals as highly efficient light emitters as they possess high photoluminescence (PL) quantum yields,[11,12] relatively short PL lifetimes,[13] and better stability.[14] However, the nanocrystals are not quite ideal for studying the intrinsic properties of halide perovskites because they are sensitive to surface defects with a high surface to volume ratio,[15] and thin films are influenced by substrates[16] and grain boundaries.[17] Obviously, a single crystal seems more suitable for analyzing the pristine optical properties of these materials with minimal extrinsic effects. Intriguingly, however, the optical behavior of a perovskite single crystal is complicated by an additional feature in the low-energy tail of PL emission[5,18−20] arising from a cascade of emission and reabsorption[21] in the bulk, namely, photon recycling.[22] The resulting dual-peak feature often led to the incorrect concept of above-band-gap emission,[23−26] whereas strong reabsorption renders the typical carrier dynamics unreliable. In fact, there have been several attempts to explain the nontrivial carrier dynamics in perovskite single crystals by including fast diffusion of carriers into the interior,[27−29] but there exists a wide variance in dynamic parameters that are strongly model dependent.

Photon recycling requires a subgap state to cause dual-gap emission of the PL in halide perovskites. Although typical

Received: August 25, 2020

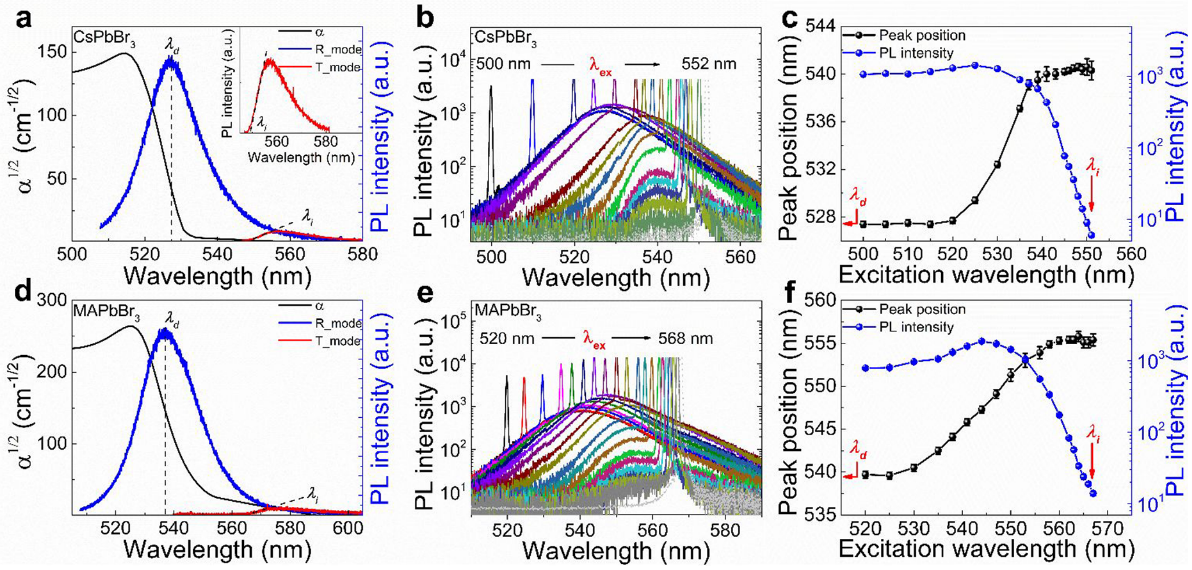

Figure 1. Absorption (black) and PL spectra from (a) CsPbBr$_3$ and (d) MAPbBr$_3$ obtained under R mode (blue) and T mode (red) at 300 K when excited at λ_{ex} = 500 nm. The wavelengths for the indirect and direct gaps are denoted by λ_i and λ_d, respectively. Semilog plot of the series of room-temperature PL spectra from (b) CsPbBr$_3$ and (e) MAPbBr$_3$ obtained using PLE spectroscopy. The PL peak position (black spheres) and the PL intensity (blue spheres) as a function of λ_{ex} at 300 K determined by the PLE data.

Urbach tailing can serve as a subgap state, an alternative mechanism was recently proposed to account for the dual nature in terms of an additional indirect transition allowed by the dynamic Rashba effect.[18] When a nonzero electric field is generated by inversion symmetry breaking, the spin of a free charge couples to an effective magnetic field by strong spin–orbit coupling (SOC), causing spin-dependent energy band splitting to form an indirect gap slightly below the direct band edge. Surprisingly, despite the presence of an inversion center, evidence for Rashba splitting has been reported in halide perovskites by computational simulations,[30−32] circular photogalvanic effect,[33] spin-polarization dependence,[18] optical Hanle effect,[34] and so on. Currently, there are various views on the origin for broken inversion symmetry, which are categorized into dynamic effects[18,33,35−37] (arising from dynamic lattice distortion on a 100 fs time scale[38,39]) and static effects (arising from static inversion symmetry breaking).[34,39−41] Theoretically, the dynamic Rashba effect was first proposed in 2016,[35] whereas the static Rashba effect is also possible at the surface of the crystal.[32] While the dynamic Rashba effect is predicted to exist in both AIHPs and OIHPs,[30] the issue remains controversial.

In this paper, we aim to identify and even control the underlying mechanisms for inversion symmetry breaking that cause both dynamic and static Rashba effects in high-quality single crystals based on a series of precision spectroscopic measurements, which include nonlinear optical multiphoton absorption and harmonic generation. First, we precisely pinpointed the location of the indirect gap by fine-scale photoluminescence excitation (PLE) spectroscopy over a wide temperature range from 10 to 300 K. The degree of Rashba splitting was assessed by the energy difference between the direct gap and the indirect gap,[18] which shrinks with decreasing temperature. While the dynamic Rashba effect persists in MAPbBr$_3$, we confirmed that it essentially vanishes in CsPbBr$_3$ below 50 K, which is also evidenced by the recovery of the color purity of the crystal. This in turn causes a significant increase in the PL brightness via suppression of photon recycling in the dynamic Rashba gap. We found that the dynamic Rashba effect is critically dependent on the type of the A-site cation (Cs or MA), and the origin for dynamic inversion symmetry breaking arises most likely from the thermal motion of the cation in the perovskite cage. Then we showed that the static Rashba effect develops only in MAPbBr$_3$ at low temperatures (<90 K) based on temperature- and polarization-dependent PL spectroscopy. The degree of circular polarization in MAPbBr$_3$ increases at lower temperature and can be as high as ∼3% at 10 K. The origin for static inversion symmetry breaking is local reconstruction of the surface via MA-cation ordering, which is most significant across a few layers from the crystal surface to the interior as corroborated by nonlinear optical measurements. We further demonstrate that this static effect in the OIHP can be completely quenched by a simple surface treatment using polymethyl methacrylate (PMMA) coating. We emphasize that our results do not show any evidence of Rashba splitting by extrinsic effects due to defects or imperfections and therefore provide a rationale for both dynamic and static Rashba effects in this important class of materials in pristine quality. We believe that our fundamental results have implications in the role of halide perovskites in the emerging field of spin-optoelectronics, which is a combination of spintronics and optoelectronics.[34,42]

■ RESULTS AND DISCUSSION

Our CsPbBr$_3$ and MAPbBr$_3$ single crystals were synthesized by the Bridgman[14] and inverse temperature crystallization (ITC) methods,[43] respectively. The sample preparation procedure and X-ray diffraction results (Figure S1) are detailed in the Supporting Information. Figure 1a and 1d shows the absorption (black) and the PL spectra from CsPbBr$_3$ and MAPbBr$_3$, respectively, obtained at 300 K under reflection geometry (R mode, blue) and transmission geometry (T mode, red). The corresponding excitation wavelength (λ_{ex}) for one-photon absorption (1PA) was 500 nm. The intensity dependence of the PL clearly indicates that it arises from

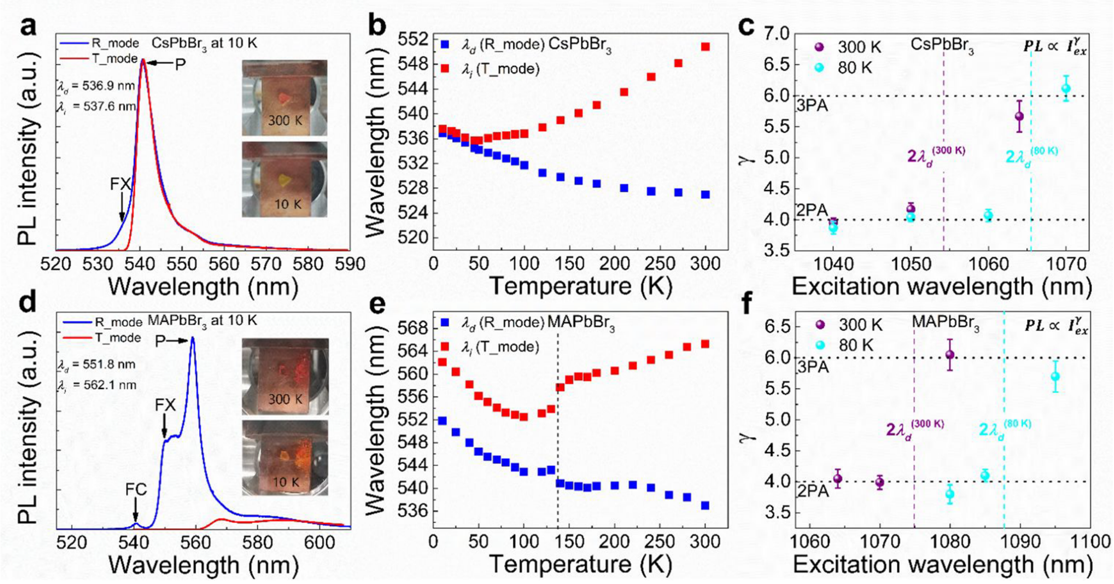

Figure 2. PL spectra from (a) CsPbBr$_3$ and (d) MAPbBr$_3$ at 10 K obtained under the R mode (blue) and the T mode (red). (Inset) Representative photographs of the single crystals at 300 and 10 K. Apparent color change in CsPbBr$_3$ is associated with quenching of the dynamic Rashba effect. Temperature-dependent λ_d (blue squares) and λ_i (red squares) of (b) CsPbBr$_3$ and (e) MAPbBr$_3$ at λ_{ex} = 500 nm. Dashed line indicates the phase-transition temperature for MAPbBr$_3$ around 140 K. Power exponent (γ) of the intensity-dependent PL vs λ_{ex} for (c) CsPbBr$_3$ and (f) MAPbBr$_3$ at 80 and 300 K, where the boundaries for 2PA and 3PA are indicated by the cyan dashed line (80 K) and the purple dashed line (300 K), respectively. γ values of ~4 for 2PA and ~6 for 3PA indicate that the PL arises from carrier recombination at high temperatures (>80 K).

radiative recombination of free carriers at room temperature (Figure S2). The peak position (λ_d) of the blue trace coincides with the absorption edge, which corresponds to the wavelength for the fundamental direct gap of each single crystal; at low temperatures where excitons are dominant, λ_d corresponds to the wavelength for the exciton PL, i.e., the optical gap that is slightly below the direct gap by exciton binding energy.

Under the T mode, however, a completely different PL (red trace) was obtained from each sample in terms of both peak position and brightness. This drastic change in the PL arises from effective reabsorption of the main PL while traveling a macroscopic distance before exiting the sample (thickness ≈ 2 mm). We attribute the origin for this subgap absorption to the indirect Rashba gap arising from dynamic inversion symmetry breaking in accordance with ref 33 and as further explained below through its temperature dependence (Figure 2). Hence, the high-energy onset of the red trace was assigned to λ_i, which corresponds to the wavelength for the indirect gap formed slightly below the direct gap. This implies that the single crystal is truly transparent above λ_i (below the Rashba gap). It is interesting that the dynamic Rashba gap can be measured by time-integrated absorption or PL experiments because dynamic inversion symmetry breaking is always present throughout the random thermal distortion of the perovskite cage. However, we found that this dynamic effect can be discerned by neither circular polarization spectroscopy nor second harmonic generation (SHG) as they have directional dependence, which would be averaged out for the random thermal motion. It is noteworthy that the main PL (blue trace) is spectrally asymmetric because of low-energy tailing, which indeed coincides with the red trace. This dual-peak nature obtained under the R mode therefore consists of a symmetric band-to-band transition and the additional PL resulting from photon recycling via successive emission and reabsorption of the main PL directed into the interior of the sample. As described later, the low-energy peak intensity strongly depends on the sample thickness (Figure 5). This indicates that the secondary peak is not a simple indirect emission but ambient PL after photon recycling through the dynamic Rashba gap.

In order to determine the precise locations for λ_d and λ_i, we performed fine-scale PLE spectroscopy on our single crystals. Figure 1b and 1e shows the series of the PL spectra from CsPbBr$_3$ and MAPbBr$_3$, respectively, plotted on a semi-logarithmic (semilog) scale when λ_{ex} was varied from λ_i to λ_d. The sharp peak on top of each PL spectrum corresponds to the scattered laser light registered as a peak by our detection system, where its intensity was cut down by more than a factor of 100 with orthogonal polarization control. Interestingly, both single crystals yield a weak indirect PL when λ_{ex} is resonant with the Rashba gap, i.e., $\lambda_{ex} = \lambda_i$. When λ_{ex} was varied from the Rashba onset to the direct gap, the PL intensity steeply increases and its peak position blue shifts toward the direct gap until the peak position saturates into a constant wavelength, which is λ_d. In Figure 1c and 1f, we plot the corresponding PL peak position (black spheres) and the PL intensity (blue spheres) as a function of λ_{ex} as determined from Figure 1b and 1e. The values for λ_d are 527 (~2.35 eV) and 539 nm (~2.30 eV) for CsPbBr$_3$ and MAPbBr$_3$, respectively, at 300 K. These band-gap wavelengths are consistent with values for λ_d shown in Figure 1a and 1d. The values for λ_i were determined from the onset λ_{ex}, causing the weak indirect PL, which are 551 (2.25 eV) and 567 nm (~2.19 eV) for CsPbBr$_3$ and MAPbBr$_3$, respectively, at 300 K. These indirect-gap wavelengths are consistent with the values for λ_i shown in Figure 1a and 1d. This implies that the PL spectra using the R and T modes can be utilized for estimating λ_d and λ_i. On the basis of the difference between λ_i and λ_d, we conclude that Rashba splitting is about 10% larger for the OIHP single crystal.

In order to study the temperature dependence of the dynamic Rashba effect, we measured the PL as a function of temperature from 300 to 10 K (Figures S3−S5). For instance, in Figure 2a and 2d, we plot the PL obtained from CsPbBr$_3$

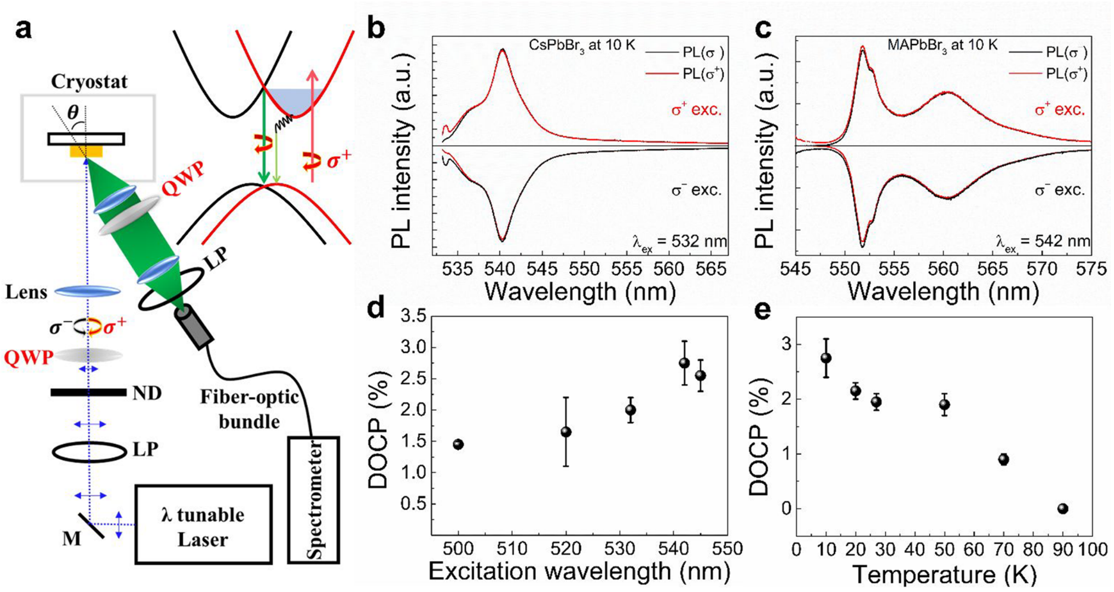

Figure 3. (a) Experimental setup for the DOCP measurement using the scattering geometry ($\theta \approx 20°$) to remove the polarization dependence of a beam splitter, where M is a mirror, ND is a neutral-density filter, QWPs are quarter waveplates, and LPs are linear polarizers. (Inset) Schematic of the Rashba-split conduction and valence bands with spin-dependent selective optical transition for circularly polarized light (σ^+) near the band gap (E_g). Right/left circularly polarized PL (σ^-)/PL (σ^+) under σ^-/σ^+ excitation from (b) $CsPbBr_3$ and (c) $MAPbBr_3$ at 10 K. Only $MAPbBr_3$ exhibits a finite DOCP near the direct-gap peak (552 nm). (d) λ_{ex}-dependent DOCP of $MAPbBr_3$ at 10 K. (e) Temperature-dependent DOCP of $MAPbBr_3$ by tuning λ_{ex} being ~10 nm above the exciton PL line.

and $MAPbBr_3$, respectively, at 10 K under the R mode (blue) and the T mode (red). At this low temperature, the nature of the PL is essentially excitonic (X) since the exciton binding energy is much larger than the thermal energy (~0.9 meV).[44,45] However, we found that $MAPbBr_3$ exhibits a small but measurable free-carrier peak (FC) even at 10 K, which requires further investigation in the future. In both single crystals, the so-called P-band emission (P) is dominant, which occurs near the polariton bottleneck which is slightly below the X line as a consequence of inelastic exciton−exciton scattering.[46,47] Note that the effect of reabsorption is significantly suppressed in $CsPbBr_3$, as indicated by the coincidence between the blue and the red traces across the Rashba gap in Figure 2a. Interestingly, this is accompanied by the striking color change of the crystal from pale orange (300 K) to transparent yellow (10 K) as shown in the inset. The color change arises from the recovery of the true color of the sample without additional absorption of ambient light by the indirect Rashba gap. In contrast, $MAPbBr_3$ does not exhibit a significant color change at 10 K, implying that the dynamic Rashba effect persists at this low temperature. Therefore, there exists reabsorption of the PL in $MAPbBr_3$, causing a clear difference in the blue and red traces in Figure 2d. The estimated values for λ_d and λ_i are 536.9 and 537.6 nm in $CsPbBr_3$ and 551.8 and 562.1 nm in $MAPbBr_3$, respectively.

In Figure 2b and 2e, we plot λ_d (blue squares) and λ_i (red squares) of $CsPbBr_3$ and $MAPbBr_3$, respectively, as a function of temperature based on the PL spectra shown in Figures 2a, 2d, S3, and S4. As mentioned, the Rashba gap essentially vanishes in $CsPbBr_3$ below 50 K ($\lambda_i - \lambda_d < 1$ nm), whereas in $MAPbBr_3$ it remains almost a constant ($\lambda_i - \lambda_d \approx 10$ nm) below the dashed line (~140 K), where a structural phase transition[26] occurs from the tetragonal phase to the orthorhombic phase. A sudden change in $\lambda_i - \lambda_d$ across the dashed line seems to indicate that dynamic inversion symmetry breaking is less pronounced in the orthorhombic structure having a lower symmetry. Except for this complication arising from the phase transition in $MAPbBr_3$, both single crystals undergo a monotonic band-gap red shift as temperature decreases, which is typical for halide perovskites.[18,48] However, it should be noted that the temperature dependence of the indirect gap (λ_i) is not related to any band-gap-shift model, such as the Varshni equation,[49] as it solely reflects the degree of the dynamic Rashba effect. A drastically different behavior observed at low temperatures shows that dynamic inversion symmetry breaking is contingent upon the type of the A-site cation (Cs or MA) and arises most likely from the thermal motion of the cation in the perovskite cage. It is also evident that the dynamic Rashba effect is more prominent in $MAPbBr_3$ due to the polar character of the MA cation compared with the much more symmetric Cs cation in $CsPbBr_3$.

We performed nonlinear optical multiphoton absorption spectroscopy across the boundary between two-photon absorption (2PA) and three-photon absorption (3PA) for the perovskite crystals and examined the excitation power dependences at two representative temperatures of 300 and 80 K (see, for example, Figures S6 and S7 for $CsPbBr_3$). Here, we emphasize that the multiphoton absorption order must be defined in terms of λ_d, not λ_i.[23] The purple and cyan dashed lines in Figure 2c and 2f correspond to the 2PA−3PA boundaries for $CsPbBr_3$ and $MAPbBr_3$ at 300 and 80 K, respectively. The purple spheres (300 K) and cyan spheres (80 K) correspond to the power exponents (γ's) for the selected excitation wavelengths, indicating that the PL arises from radiative recombination of free carriers as γ values are about 4 for 2PA (left side of the dashed lines) and 6 for 3PA (right side of the dashed lines), respectively. We found that a minor deviation from the precise power law is due to the saturation effect of the carriers during the pulse time (30 ps).[47]

Under strong SOC and inversion symmetry breaking, the spin degeneracy of the valence band (VB) and the conduction band (CB) can be removed. In this situation, selective optical excitation of a specific spin band can be realized using right/left circularly polarized light (RCP/LCP, σ^-/σ^+). Splitting of the VB (CB) is mainly caused by hybridization of the Br 4p and Pb 6s orbitals (Pb 6p orbitals), causing a larger splitting in the CB than the VB as schematically depicted in the inset of Figure 3a.[32,50] Therefore, the presence of Rashba splitting can be confirmed by measuring the degree of circular polarization (DOCP) given by

$$\mathrm{DOCP}\ (\%) = \left| \frac{\mathrm{PL}(\sigma^+) - \mathrm{PL}(\sigma^-)}{\mathrm{PL}(\sigma^+) + \mathrm{PL}(\sigma^-)} \right| \times 100 \tag{1}$$

where $\mathrm{PL}(\sigma^-)$ and $\mathrm{PL}(\sigma^+)$ are the measured PL intensities having RCP and LCP, respectively. Considering a fast spin relaxation time due to strong SOC in halide perovskites, the DOCP would be most visible when employed to the case for time-resolved excitation[51,52] but can be certainly used for our time-integrated PL spectroscopy. However, it should be noted that the dynamic Rashba effect would yield DOCP = 0% in the time-integrated regime, since the orientation of spins is random under thermal distortion of the lattice. Therefore, in our experimental configuration, a nonzero DOCP would be a smoking gun for the static Rashba effect, where the origin for inversion symmetry breaking is systematic, not thermal.

Figure 3a illustrates our experimental setup for polarization-dependent PL spectroscopy to assess the DOCP of the perovskites using a pair of quarter waveplates (QWP's) (see the Supporting Information for details). Compared with a typical setup using a beam splitter, we collected the PL signal under scattering geometry ($\theta \approx 20°$) in order to entirely eliminate the beam-splitting efficiency that depends on polarization as well as wavelength. In Figure 3b we plot the PL spectra from $CsPbBr_3$ using λ_{ex} = 532 nm, which is ∼10 nm above the exciton PL line at 10 K, where the trace in the upper (lower) panel corresponds to the PL excited by σ^+ (σ^-) polarization and the red (black) trace is the PL detected using σ^+ (σ^-) polarization. In other words, the red (black) PL in the upper panel corresponds to the parallel (orthogonal) polarization scheme, and the color code reverses in the lower panel. Ideally, the PL pair with different colors in the upper and lower panels should be a mirror image of each other. Throughout careful analyses on the series of the PL data averaged over laser fluctuation we confirmed that the DOCP is zero in our AIHP single crystal over the entire temperature range (Figure S8). Hence, there is no static inversion symmetry breaking in $CsPbBr_3$. In fact, we did not find any evidence for extrinsic symmetry-breaking sources such as defects or impurities to cause a measurable static Rashba effect, thereby signifying the quality of our specimen.

However, our OIHP single crystal exhibits a small but finite DOCP (∼3%) near the exciton PL at 10 K as shown in Figure 3c, in which λ_{ex} was tuned to 542 nm in order to ensure the same excitation condition, i.e., being ∼10 nm above the main exciton PL line. We emphasize that DOCP should be assessed at the direct transition as it is zero for indirect transition involving incoherent phonon scattering. Most importantly, we confirmed that this finite DOCP is always reproducible over any excitation spot on the sample, clearly demonstrating the presence of a static Rashba effect. This static effect can be more clearly seen via the PL contrast between the parallel and the orthogonal polarization as shown in Figure S9, which plots $|\mathrm{PL}(\sigma^+) - \mathrm{PL}(\sigma^-)|$. We also measured the DOCP of $MAPbBr_3$ as a function of λ_{ex} and temperature as well (Figures S10 and S11). The dots in Figure 3d correspond to the DOCP values at 10 K for several excitation wavelengths, showing that DOCP increases up to nearly 3% when λ_{ex} was tuned toward the main PL. This effect can be understood in terms of an available phase space for spin flip and indeed is observed in the recent work.[18] Figure 3e depicts the DOCP values (dots) of $MAPbBr_3$ as a function of temperature. DOCP assumes the maximum value of ∼3% at the lowest temperature but monotonically decreases with increasing temperature and vanishes at 90 K. Therefore, we conclude that the OIHP exhibits both dynamic and static Rashba effects, where the latter is present at low temperatures, <90 K.

The origin for the static inversion symmetry breaking is currently being debated by several candidates: (i) ferroelectric structure,[40] (ii) anharmonic thermal fluctuation between the organic cation and $PbBr_6$,[18,33,35−37] (iii) MA dipole alignment at low temperature,[34] (iv) structural surface relaxation,[53] and so on. We measured the SHG response from the single crystals at 10 K at λ_{ex} = 1500 nm as SHG is sensitive to static inversion symmetry breaking in the crystalline phase. More specifically, our picosecond excitation setup is ideal for sensing bulk SHG only,[54] in which a 30 ps pulse is too weak in input intensity to cause surface SHG arising from the single boundary layer compared with a typical femtosecond setup. As predicted, $CsPbBr_3$ does not exhibit any SHG (Figure 4a), consistent with zero DOCP. Intriguingly, however, it turns out that $MAPbBr_3$ does not yield any measurable SHG response (black) either as shown in Figure 4b. The absence of bulk SHG was further confirmed by the strong third harmonic generation (THG) response (red), which is a higher order nonlinear optical process and generally weaker than SHG by orders of magnitude in typical noncentrosymmetric crystals. Therefore,

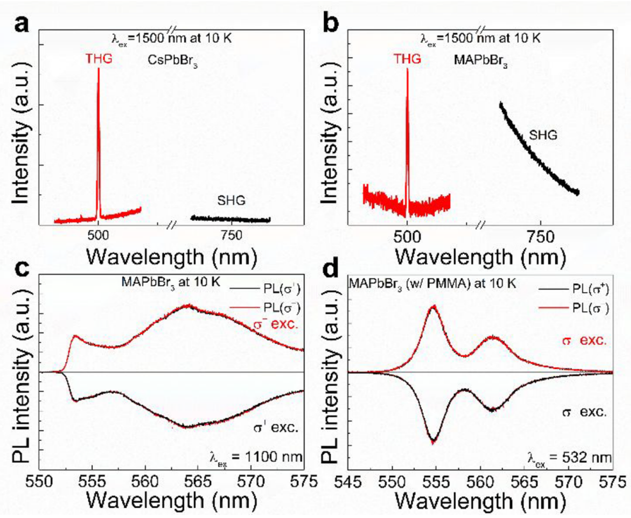

Figure 4. SHG (black) and THG (red) responses from (a) $CsPbBr_3$ and (b) $MAPbBr_3$ at 10 K and λ_{ex} = 1500 nm. In the case of $MAPbBr_3$, the black trace corresponds to the low-energy tail of 2PA-induced PL. Right/left circularly polarized $\mathrm{PL}(\sigma^-)/\mathrm{PL}(\sigma^+)$ under σ^-/σ^+ excitation from (c) $MAPbBr_3$ using resonant 2PA and (d) PMMA-coated $MAPbBr_3$ using typical 1PA at 10 K. For 2PA, we intentionally formed the focus at the interior of the single crystal to ensure bulk excitation.

the origin for static inversion symmetry breaking in the OIHP single crystal should be essentially surface induced. The surface-induced static effect was further evidenced by zero DOCP under resonant 2PA (Figure 4c), which directly generates cold excitons with well-defined spin orientation in the bulk. Note here that resonant excitation to the exciton line would yield the maximum DOCP in accordance with Figure 3d. Therefore, zero DOCP even under resonant 2PA unambiguously demonstrates that the perovskite crystallizes into a centrosymmetric structure inside the OIHP single crystal, and therefore, static inversion symmetry breaking should originate from the surface. However, the origin cannot be simply the boundary surface between the sample and the ambient, which is present at all temperatures and even in $CsPbBr_3$. Clearly, our results eliminate the candidates i, ii, and iii. We emphasize that candidate ii is indeed the mechanism for the dynamic Rashba effect, which is more prevalent at higher temperatures, whereas the static Rashba effect in Figure 3c only occurs at temperatures lower than 90 K. On the basis of density functional theory calculations, it was recently suggested that surface reconstruction by the MA cation ordering can give rise to a static Rashba effect at low temperatures.[53] This localized inversion symmetry breaking is most significant from the boundary surface to a few layers into the interior of the crystal, where the degree of freedom for the MA-cation motion is relatively higher than that in the bulk. In order to prove the feasibility of the model, we prepared a single crystal of $MAPbBr_3$ coated with PMMA. Quite interestingly, we confirmed that the PMMA-coated $MAPbBr_3$ did not show any static Rashba effect (Figure 4d), in a sharp contrast with the pristine crystal of $MAPbBr_3$, yielding a finite DOCP value (Figure 3c). We believe that PMMA passivates the surface defects[55] and constrains MA cations by hydrogen bonding between the cations and the capping polymers.[56] In fact, the bound exciton peak observed slightly below the main exciton PL in Figure 3c is suppressed by surface trap passivation upon PMMA coating. Our observation therefore indicates that the source for static inversion symmetry breaking at the surface is the candidate iv, surface reconstruction. In fact, low-temperature surface reconstruction was recently observed in $MAPbBr_3$ by real-space imaging.[57] Although PMMA coating can passivate surface defects, we can neglect the impact of surface defects on the static Rashba effect simply because of the absence of Rashba splitting in $CsPbBr_3$. In other words, if surface defects are the main mechanism, $CsPbBr_3$ should also exhibit a static Rashba effect as halide vacancy is ubiquitous on the surface of perovskites.[15,58] The role of surface recombination and its temperature dependence is discussed further in the Supporting Information (Figure S12 and analysis of TRPL data).

Lastly, we examined the impact of the crystal size on photon recycling in the indirect band gap. In order to clearly confirm the effect, we carried out polarization-dependent PL spectroscopy on the bulk and powder (~100 μm) samples at 150 K, where the static Rashba effect is absent (DOCP = 0). In Figure 5a, 5b, 5c, and 5d, we plot the right/left circularly polarized $PL(\sigma^-)/PL(\sigma^+)$ from bulk $CsPbBr_3$, $CsPbBr_3$ powder, bulk $MAPbBr_3$, and $MAPbBr_3$ powder, respectively, at 150 K under σ^-/σ^+ excitation. Our results clearly show that the secondary peak can significantly alter the PL spectrum depending on the degree of photon recycling in both AIHP and OIHP single crystals. Compared with the bulk counterparts, small-sized powders yield the more pronounced peak below the direct gap due to less steps of reabsorption and reemission. This effect is schematically illustrated in Figure 5e.

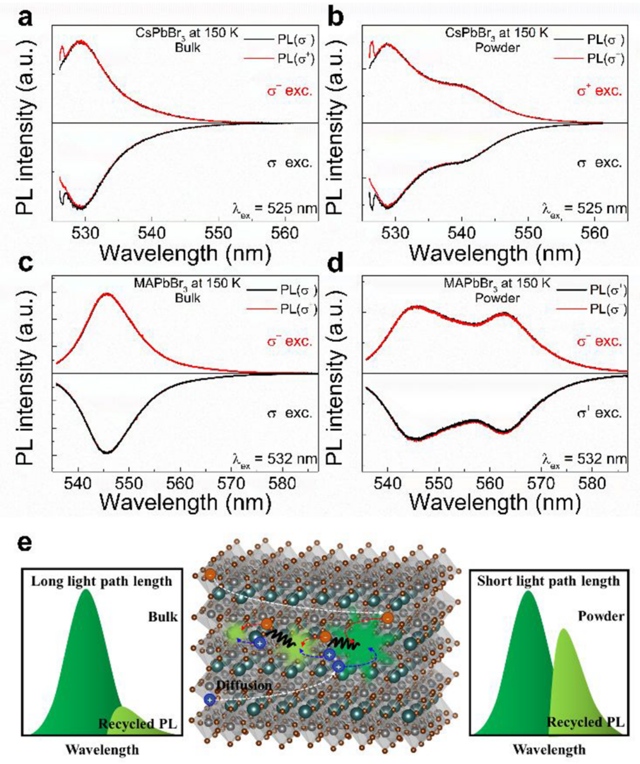

Figure 5. Right/left circularly polarized $PL(\sigma^-)/PL(\sigma^+)$ under σ^-/σ^+ excitation from (a) bulk $CsPbBr_3$, (b) $CsPbBr_3$ powder, (c) bulk $MAPbBr_3$, and (d) $MAPbBr_3$ powder at 150 K, where DOCP = 0. Indirect transition is more pronounced in powders (smaller in size) due to less efficient photon recycling. (e) Schematic diagram for the photon-recycling effect: PL undergoes more recycling steps for the longer PL path.

■ CONCLUSION

We thoroughly investigated both the dynamic and the static Rashba effects in bromide AIHP and OIHP single crystals. Both perovskite single crystals exhibit a dynamic Rashba effect as evidenced by formation of the indirect gap via thermal distortion of the lattice. While the effect persists in $MAPbBr_3$, dynamic Rashba splitting in $CsPbBr_3$ disappears at low temperatures (<50 K), which is accompanied by the apparent color change of the crystal. On the basis of circularly polarized PL spectroscopy, we also examined the static Rashba effect and found that only $MAPbBr_3$ exhibits a static Rashba effect with DOCP ≈ 3% at 10 K. The static inversion symmetry breaking occurs near the surface, not bulk, as confirmed by nonlinear optical harmonic generation and 2PA. We identified that the underlying mechanism for the static Rashba effect is most likely surface reconstruction of MA cations, which was theoretically predicted and experimentally confirmed recently.[53,57] Considering the surface nature of the effect and a relatively fast spin decoherence time of ~2 ps in bulk perovskite crystals,[52] we believe that a time-integrated DOCP of 3% is a rather large value. We also demonstrated that the static Rashba effect in the OIHP can be actively controlled by a simple surface treatment with PMMA, which suppresses the degree of freedom for MA-cation ordering. Finally, the PL spectrum can be significantly affected by photon recycling via the dynamic Rashba gap depending on the crystal size. Our results indicate that the Rashba effect is less prone to extrinsic defects We believe that our results are important for furthering the halide perovskites into the emerging field of spin-optoelectronics.

■ ASSOCIATED CONTENT

Supporting Information

The Supporting Information is available free of charge at https://pubs.acs.org/doi/10.1021/jacs.0c09132.

Experimental details, XRD data, time-integrated PL spectra, and time-resolved PL spectra (PDF)

■ AUTHOR INFORMATION

Corresponding Author

Joon I. Jang − *Department of Physics, Sogang University, Seoul 04107, South Korea;* orcid.org/0000-0002-1608-8321; Email: jjcoupling@sogang.ac.kr

Authors

Hongsun Ryu − *Department of Physics, Sogang University, Seoul 04107, South Korea*

Dae Young Park − *Department of Energy Science, Sungkyunkwan University, Suwon 16419, South Korea*

Kyle M. McCall − *Department of Chemistry, Northwestern University, Evanston, Illinois 60208, United States; Laboratory of Inorganic Chemistry, Department of Chemistry and Applied Biosciences, ETH Zurich, Zurich 8093, Switzerland; Laboratory for Thin Films and Photovoltaics, Empa-Swiss Federal Laboratories for Materials Science and Technology, Dübendorf CH-8600, Switzerland*

Hye Ryung Byun − *Department of Physics, Sogang University, Seoul 04107, South Korea*

Yongjun Lee − *Department of Energy Science, Sungkyunkwan University, Suwon 16419, South Korea*

Tae Jung Kim − *Department of Physics, Kyung Hee University, Seoul 02447, South Korea*

Mun Seok Jeong − *Department of Energy Science, Sungkyunkwan University, Suwon 16419, South Korea;* orcid.org/0000-0002-7019-8089

Jeongyong Kim − *Department of Energy Science, Sungkyunkwan University, Suwon 16419, South Korea;* orcid.org/0000-0003-4679-0370

Mercouri G. Kanatzidis − *Department of Chemistry, Northwestern University, Evanston, Illinois 60208, United States;* orcid.org/0000-0003-2037-4168

Complete contact information is available at: https://pubs.acs.org/10.1021/jacs.0c09132

Notes

The authors declare no competing financial interest.

■ ACKNOWLEDGMENTS

This work was supported by the Basic Science Research Programs (2017R1D1A1B03035539 and 2020R1F1A1069646) through the National Research Foundation of Korea (NRF), funded by the Korean government. At Northwestern this work was supported by the US Department of Energy, Office of Science, Basic Energy Sciences, under Grant No. SC0012541 (synthesis and structural characterization).

■ REFERENCES

(1) Green, M. A.; Ho-Baillie, A.; Snaith, H. J. The Emergence of Perovskite Solar Cells. *Nat. Photonics* **2014**, *8*, 506−514.

(2) Kang, J.; Wang, L. W. High Defect Tolerance in Lead Halide Perovskite $CsPbBr_3$. *J. Phys. Chem. Lett.* **2017**, *8*, 489−493.

(3) Protesescu, L.; Yakunin, S.; Bodnarchuk, M. I.; Krieg, F.; Caputo, R.; Hendon, C. H.; Yang, R. X.; Walsh, A.; Kovalenko, M. V. Nanocrystals of Cesium Lead Halide Perovskites ($CsPbX_3$, X = Cl, Br, and I): Novel Optoelectronic Materials Showing Bright Emission with Wide Color Gamut. *Nano Lett.* **2015**, *15*, 3692−3696.

(4) Byun, H. R.; Park, D. Y.; Oh, H. M.; Namkoong, G.; Jeong, M. S. Light Soaking Phenomena in Organic-Inorganic Mixed Halide Perovskite Single Crystals. *ACS Photonics* **2017**, *4*, 2813−2820.

(5) Fang, Y.; Dong, Q.; Shao, Y.; Yuan, Y.; Huang, J. Highly Narrowband Perovskite Single-Crystal Photodetectors Enabled by Surface-Charge Recombination. *Nat. Photonics* **2015**, *9*, 679−686.

(6) Shi, D.; Adinolfi, V.; Comin, R.; Yuan, M.; Alarousu, E.; Buin, A.; Chen, Y.; Hoogland, S.; Rothenberger, A.; Katsiev, K.; Losovyj, Y.; Zhang, X.; Dowben, P. A.; Mohammed, O. F.; Sargent, E. H.; Bakr, O. M. Low Trap-State Density and Long Carrier Diffusion in Organolead Trihalide Perovskite Single Crystals. *Science* **2015**, *347*, 519−522.

(7) Rakita, Y.; Kedem, N.; Gupta, S.; Sadhanala, A.; Kalchenko, V.; Böhm, M. L.; Kulbak, M.; Friend, R. H.; Cahen, D.; Hodes, G. Low-Temperature Solution-Grown $CsPbBr_3$ Single Crystals and Their Characterization. *Cryst. Growth Des.* **2016**, *16*, 5717−5725.

(8) Zhang, H.; Liu, X.; Dong, J.; Yu, H.; Zhou, C.; Zhang, B.; Xu, Y.; Jie, W. Centimeter-Sized Inorganic Lead Halide Perovskite $CsPbBr_3$ Crystals Grown by an Improved Solution Method. *Cryst. Growth Des.* **2017**, *17*, 6426−6431.

(9) Dong, Q.; Fang, Y.; Shao, Y.; Mulligan, P.; Qiu, J.; Cao, L.; Huang, J. Electron-Hole Diffusion Lengths > 175 μm in SolutionGrown $CH_3NH_3PbI_3$ Single Crystals. *Science* **2015**, *347*, 967−970.

(10) Stranks, S. D.; Eperon, G. E.; Grancini, G.; Menelaou, C.; Alcocer, M. J. P.; Leijtens, T.; Herz, L. M.; Petrozza, A.; Snaith, H. J. Electron-Hole Diffusion Lengths Exceeding 1 Micrometer in an Organometal Trihalide Perovskite Absorber. *Science* **2013**, *342*, 341−344.

(11) Pan, J.; Shang, Y.; Yin, J.; De Bastiani, M.; Peng, W.; Dursun, I.; Sinatra, L.; El-Zohry, A. M.; Hedhili, M. N.; Emwas, A. H.; Mohammed, O. F.; Ning, Z.; Bakr, O. M. Bidentate Ligand-Passivated CsPbI 3 Perovskite Nanocrystals for Stable Near-Unity Photoluminescence Quantum Yield and Efficient Red Light-Emitting Diodes. *J. Am. Chem. Soc.* **2018**, *140*, 562−565.

(12) Wang, S.; Bi, C.; Yuan, J.; Zhang, L.; Tian, J. Original Core-Shell Structure of Cubic $CsPbBr_3$@Amorphous $CsPbBr_x$ Perovskite Quantum Dots with a High Blue Photoluminescence Quantum Yield of over 80%. *ACS Energy Lett.* **2018**, *3*, 245−251.

(13) Song, J.; Cui, Q.; Li, J.; Xu, J.; Wang, Y.; Xu, L.; Xue, J.; Dong, Y.; Tian, T.; Sun, H.; Zeng, H. Ultralarge All-Inorganic Perovskite Bulk Single Crystal for High-Performance Visible−Infrared Dual-Modal Photodetectors. *Adv. Opt. Mater.* **2017**, *5*, 1700157.

(14) Stoumpos, C. C.; Malliakas, C. D.; Peters, J. A.; Liu, Z.; Sebastian, M.; Im, J.; Chasapis, T. C.; Wibowo, A. C.; Chung, D. Y.; Freeman, A. J.; Wessels, B. W.; Kanatzidis, M. G. Crystal Growth of the Perovskite Semiconductor $CsPbBr_3$: A New Material for High-Energy Radiation Detection. *Cryst. Growth Des.* **2013**, *13*, 2722−2727.

(15) Wang, Y.; Ren, Y.; Zhang, S.; Wu, J.; Song, J.; Li, X.; Xu, J.; Sow, C. H.; Zeng, H.; Sun, H. Switching Excitonic Recombination and Carrier Trapping in Cesium Lead Halide Perovskites by Air. *Commun. Phys.* **2018**, *1*, 96.

(16) Zhao, J.; Deng, Y.; Wei, H.; Zheng, X.; Yu, Z.; Shao, Y.; Shield, J. E.; Huang, J. Strained Hybrid Perovskite Thin Films and Their Impact on the Intrinsic Stability of Perovskite Solar Cells. *Sci. Adv.* **2017**, *3*, No. eaao5616.

(17) Doherty, T. A. S.; Winchester, A. J.; Macpherson, S.; Johnstone, D. N.; Pareek, V.; Tennyson, E. M.; Kosar, S.; Kosasih, F. U.; Anaya, M.; Abdi-Jalebi, M.; Andaji-Garmaroudi, Z.; Wong, E. L.; Madéo, J.; Chiang, Y. H.; Park, J. S.; Jung, Y. K.; Petoukhoff, C. E.; Divitini, G.;

Man, M. K. L.; Ducati, C.; Walsh, A.; Midgley, P. A.; Dani, K. M.; Stranks, S. D. Performance-Limiting Nanoscale Trap Clusters at Grain Junctions in Halide Perovskites. *Nature* **2020**, *580*, 360−366.

(18) Wu, B.; Yuan, H.; Xu, Q.; Steele, J. A.; Giovanni, D.; Puech, P.; Fu, J.; Ng, Y. F.; Jamaludin, N. F.; Solanki, A.; Mhaisalkar, S.; Mathews, N.; Roeffaers, M. B. J.; Grätzel, M.; Hofkens, J.; Sum, T. C. Indirect Tail States Formation by Thermal-Induced Polar Fluctuations in Halide Perovskites. *Nat. Commun.* **2019**, *10*, 484.

(19) Murali, B.; Dey, S.; Abdelhady, A. L.; Peng, W.; Alarousu, E.; Kirmani, A. R.; Cho, N.; Sarmah, S. P.; Parida, M. R.; Saidaminov, M. I.; Zhumekenov, A. A.; Sun, J.; Alias, M. S.; Yengel, E.; Ooi, B. S.; Amassian, A.; Bakr, O. M.; Mohammed, O. F. Surface Restructuring of Hybrid Perovskite Crystals. *ACS Energy Lett.* **2016**, *1*, 1119−1126.

(20) Fang, X.; Zhang, K.; Li, Y.; Yao, L.; Zhang, Y.; Wang, Y.; Zhai, W.; Tao, L.; Du, H.; Ran, G. Effect of Excess $PbBr_2$ on Photoluminescence Spectra of $CH_3NH_3PbBr_3$ Perovskite Particles at Room Temperature. *Appl. Phys. Lett.* **2016**, *108*, 071109.

(21) Schötz, K.; Askar, A. M.; Peng, W.; Seeberger, D.; Gujar, T. P.; Thelakkat, M.; Köhler, A.; Huettner, S.; Bakr, O. M.; Shankar, K.; Panzer, F. Double Peak Emission in Lead Halide Perovskites by Self-Absorption. *J. Mater. Chem. C* **2020**, *8*, 2289−2300.

(22) Fang, Y.; Wei, H.; Dong, Q.; Huang, J. Quantification of Re-Absorption and Re-Emission Processes to Determine Photon Recycling Efficiency in Perovskite Single Crystals. *Nat. Commun.* **2017**, *8*, 14417.

(23) Saouma, F. O.; Stoumpos, C. C.; Kanatzidis, M. G.; Kim, Y. S.; Jang, J. I. Multiphoton Absorption Order of $CsPbBr_3$ as Determined by Wavelength-Dependent Nonlinear Optical Spectroscopy. *J. Phys. Chem. Lett.* **2017**, *8*, 4912−4917.

(24) Sebastian, M.; Peters, J. A.; Stoumpos, C. C.; Im, J.; Kostina, S. S.; Liu, Z.; Kanatzidis, M. G.; Freeman, A. J.; Wessels, B. W. Excitonic Emissions and Above-Band-Gap Luminescence in the Single-Crystal Perovskite Semiconductors $CsPbBr_3$ and $CsPbCl_3$. *Phys. Rev. B: Condens. Matter Mater. Phys.* **2015**, *92*, 235210.

(25) Saouma, F. O.; Park, D. Y.; Kim, S. H.; Jeong, M. S.; Jang, J. I. Multiphoton Absorption Coefficients of Organic-Inorganic Lead Halide Perovskites $CH_3NH_3PbX_3$ (X = Cl, Br, I) Single Crystals. *Chem. Mater.* **2017**, *29*, 6876−6882.

(26) Wang, K.-H.; Li, L.-C.; Shellaiah, M.; Wen Sun, K. Structural and Photophysical Properties of Methylammonium Lead Tribromide ($MAPbBr_3$) Single Crystals. *Sci. Rep.* **2017**, *7*, 13643.

(27) Wenger, B.; Nayak, P. K.; Wen, X.; Kesava, S. V.; Noel, N. K.; Snaith, H. J. Consolidation of the Optoelectronic Properties of $CH_3NH_3PbBr_3$ Perovskite Single Crystals. *Nat. Commun.* **2017**, *8*, 590.

(28) Chen, J.; Morrow, D. J.; Fu, Y.; Zheng, W.; Zhao, Y.; Dang, L.; Stolt, M. J.; Kohler, D. D.; Wang, X.; Czech, K. J.; Hautzinger, M. P.; Shen, S.; Guo, L.; Pan, A.; Wright, J. C.; Jin, S. Single-Crystal Thin Films of Cesium Lead Bromide Perovskite Epitaxially Grown on Metal Oxide Perovskite ($SrTiO_3$). *J. Am. Chem. Soc.* **2017**, *139*, 13525−13532.

(29) Bi, Y.; Hutter, E. M.; Fang, Y.; Dong, Q.; Huang, J.; Savenije, T. J. Charge Carrier Lifetimes Exceeding 15 Ms in Methylammonium Lead Iodide Single Crystals. *J. Phys. Chem. Lett.* **2016**, *7*, 923−928.

(30) Marronnier, A.; Roma, G.; Carignano, M. A.; Bonnassieux, Y.; Katan, C.; Even, J.; Mosconi, E.; De Angelis, F. Influence of Disorder and Anharmonic Fluctuations on the Dynamical Rashba Effect in Purely Inorganic Lead-Halide Perovskites. *J. Phys. Chem. C* **2019**, *123*, 291−298.

(31) Kepenekian, M.; Robles, R.; Katan, C.; Sapori, D.; Pedesseau, L.; Even, J. Rashba and Dresselhaus Effects in Hybrid Organic-Inorganic Perovskites: From Basics to Devices. *ACS Nano* **2015**, *9*, 11557−11567.

(32) Mosconi, E.; Etienne, T.; De Angelis, F. Rashba Band Splitting in Organohalide Lead Perovskites: Bulk and Surface Effects. *J. Phys. Chem. Lett.* **2017**, *8*, 2247−2252.

(33) Niesner, D.; Hauck, M.; Shrestha, S.; Levchuk, I.; Matt, G. J.; Osvet, A.; Batentschuk, M.; Brabec, C.; Weber, H. B.; Fauster, T. Structural Fluctuations Cause Spin-Split States in Tetragonal $(CH_3NH_3)PbI_3$ as Evidenced by the Circular Photogalvanic Effect. *Proc. Natl. Acad. Sci. U. S. A.* **2018**, *115*, 9509−9514.

(34) Wang, J.; Zhang, C.; Liu, H.; McLaughlin, R.; Zhai, Y.; Vardeny, S. R.; Liu, X.; McGill, S.; Semenov, D.; Guo, H.; Tsuchikawa, R.; Deshpande, V. V.; Sun, D.; Vardeny, Z. V. Spin-Optoelectronic Devices Based on Hybrid Organic-Inorganic Trihalide Perovskites. *Nat. Commun.* **2019**, *10*, 129.

(35) Etienne, T.; Mosconi, E.; De Angelis, F. Dynamical Origin of the Rashba Effect in Organohalide Lead Perovskites: A Key to Suppressed Carrier Recombination in Perovskite Solar Cells? *J. Phys. Chem. Lett.* **2016**, *7*, 1638−1645.

(36) Motta, C.; El-Mellouhi, F.; Kais, S.; Tabet, N.; Alharbi, F.; Sanvito, S. Revealing the Role of Organic Cations in Hybrid Halide Perovskite $CH_3NH_3PbI_3$. *Nat. Commun.* **2015**, *6*, 7026.

(37) Wu, X.; Tan, L. Z.; Shen, X.; Hu, T.; Miyata, K.; Trinh, M. T.; Li, R.; Coffee, R.; Liu, S.; Egger, D. A.; et al. Light-Induced Picosecond Rotational Disordering of the Inorganic Sublattice in Hybrid Perovskites. *Sci. Adv.* **2017**, *3*, No. e1602388.

(38) Yaffe, O.; Guo, Y.; Tan, L. Z.; Egger, D. A.; Hull, T.; Stoumpos, C. C.; Zheng, F.; Heinz, T. F.; Kronik, L.; Kanatzidis, M. G.; Owen, J. S.; Rappe, A. M.; Pimenta, M. A.; Brus, L. E. Local Polar Fluctuations in Lead Halide Perovskite Crystals. *Phys. Rev. Lett.* **2017**, *118*, 136001.

(39) Glinka, Y. D.; Cai, R.; Li, J.; Lin, X.; Xu, B.; Wang, K.; Chen, R.; He, T.; Sun, X. W. Distinguishing between dynamical and static Rashba effects in hybrid perovskite nanocrystals using transient absorption spectroscopy. *arXiv:1909.03605*, **2019**.

(40) Rakita, Y.; Bar-Elli, O.; Meirzadeh, E.; Kaslasi, H.; Peleg, Y.; Hodes, G.; Lubomirsky, I.; Oron, D.; Ehre, D.; Cahen, D. Tetragonal $CH_3NH_3PbI_3$ Is Ferroelectric. *Proc. Natl. Acad. Sci. U. S. A.* **2017**, *114*, E5504−E5512.

(41) Park, I. H.; Zhang, Q.; Kwon, K. C.; Zhu, Z.; Yu, W.; Leng, K.; Giovanni, D.; Choi, H. S.; Abdelwahab, I.; Xu, Q. H.; Sum, T. C.; Loh, K. P. Ferroelectricity and Rashba Effect in a Two-Dimensional Dion-Jacobson Hybrid Organic-Inorganic Perovskite. *J. Am. Chem. Soc.* **2019**, *141*, 15972−15976.

(42) Odenthal, P.; Talmadge, W.; Gundlach, N.; Wang, R.; Zhang, C.; Sun, D.; Yu, Z. G.; Valy Vardeny, Z.; Li, Y. S. Spin-Polarized Exciton Quantum Beating in Hybrid Organic-Inorganic Perovskites. *Nat. Phys.* **2017**, *13*, 894−899.

(43) Saidaminov, M. I.; Abdelhady, A. L.; Murali, B.; Alarousu, E.; Burlakov, V. M.; Peng, W.; Dursun, I.; Wang, L.; He, Y.; MacUlan, G.; Goriely, A.; Wu, T.; Mohammed, O. F.; Bakr, O. M. High-Quality Bulk Hybrid Perovskite Single Crystals within Minutes by Inverse Temperature Crystallization. *Nat. Commun.* **2015**, *6*, 7586.

(44) Tilchin, J.; Dirin, D. N.; Maikov, G. I.; Sashchiuk, A.; Kovalenko, M. V.; Lifshitz, E. Hydrogen-like Wannier-Mott Excitons in Single Crystal of Methylammonium Lead Bromide Perovskite. *ACS Nano* **2016**, *10*, 6363−6371.

(45) Lozhkina, O. A.; Yudin, V. I.; Murashkina, A. A.; Shilovskikh, V. V.; Davydov, V. G.; Kevorkyants, R.; Emeline, A. V.; Kapitonov, Y. V.; Bahnemann, D. W. Low Inhomogeneous Broadening of Excitonic Resonance in MAPbBr3 Single Crystals. *J. Phys. Chem. Lett.* **2018**, *9*, 302−305.

(46) Kunugita, H.; Kiyota, Y.; Udagawa, Y.; Takeoka, Y.; Nakamura, Y.; Sano, J.; Matsushita, T.; Kondo, T.; Ema, K. Exciton-Exciton Scattering in Perovskite $CH_3NH_3PbBr_3$ Single Crystal. *Jpn. J. Appl. Phys.* **2016**, *55*, 060304.

(47) Pelant, I.; Valenta, J. *Luminescence Spectroscopy of Semiconductors*; Oxford University Press: Oxford, 2012.

(48) Frost, J. M.; Butler, K. T.; Brivio, F.; Hendon, C. H.; Van Schilfgaarde, M.; Walsh, A. Atomistic Origins of High-Performance in Hybrid Halide Perovskite Solar Cells. *Nano Lett.* **2014**, *14*, 2584−2590.

(49) Varshni, Y. P. Temperature Dependence of the Energy Gap in Semiconductors. *Physica* **1967**, *34*, 149−154.

(50) Even, J.; Pedesseau, L.; Jancu, J. M.; Katan, C. Importance of Spin-Orbit Coupling in Hybrid Organic/Inorganic Perovskites for Photovoltaic Applications. *J. Phys. Chem. Lett.* **2013**, *4*, 2999−3005.

https://dx.doi.org/10.1021/jacs.0c09132
J. Am. Chem. Soc. XXXX, XXX, XXX−XXX

(51) Giovanni, D.; Ma, H.; Chua, J.; Grätzel, M.; Ramesh, R.; Mhaisalkar, S.; Mathews, N.; Sum, T. C. Highly Spin-Polarized Carrier Dynamics and Ultralarge Photoinduced Magnetization in $CH_3NH_3PbI_3$ Perovskite Thin Films. *Nano Lett.* **2015**, *15*, 1553−1558.

(52) Chen, X.; Lu, H.; Li, Z.; Zhai, Y.; Ndione, P. F.; Berry, J. J.; Zhu, K.; Yang, Y.; Beard, M. C. Impact of Layer Thickness on the Charge Carrier and Spin Coherence Lifetime in Two-Dimensional Layered Perovskite Single Crystals. *ACS Energy Lett.* **2018**, *3*, 2273−2279.

(53) Che, X.; Traore, B.; Katan, C.; Kepenekian, M.; Even, J. Does Rashba Splitting in $CH_3NH_3PbBr_3$ Arise from 2 × 2 Surface Reconstruction? *Phys. Chem. Chem. Phys.* **2018**, *20*, 9638−9643.

(54) Stoumpos, C. C.; Cao, D. H.; Clark, D. J.; Young, J.; Rondinelli, J. M.; Jang, J. I.; Hupp, J. T.; Kanatzidis, M. G. Ruddlesden-Popper Hybrid Lead Iodide Perovskite 2D Homologous Semiconductors. *Chem. Mater.* **2016**, *28*, 2852−2867.

(55) Shao, Y.; Xiao, Z.; Bi, C.; Yuan, Y.; Huang, J. Origin and Elimination of Photocurrent Hysteresis by Fullerene Passivation in $CH_3NH_3PbI_3$ Planar Heterojunction Solar Cells. *Nat. Commun.* **2014**, *5*, 5784.

(56) Masi, S.; Rizzo, A.; Aiello, F.; Balzano, F.; Uccello-Barretta, G.; Listorti, A.; Gigli, G.; Colella, S. Multiscale Morphology Design of Hybrid Halide Perovskites through a Polymeric Template. *Nanoscale* **2015**, *7*, 18956−18963.

(57) Ohmann, R.; Ono, L. K.; Kim, H. S.; Lin, H.; Lee, M. V.; Li, Y.; Park, N. G.; Qi, Y. Real-Space Imaging of the Atomic Structure of Organic-Inorganic Perovskite. *J. Am. Chem. Soc.* **2015**, *137*, 16049−16054.

(58) Oranskaia, A.; Yin, J.; Bakr, O. M.; Brédas, J. L.; Mohammed, O. F. Halogen Migration in Hybrid Perovskites: The Organic Cation Matters. *J. Phys. Chem. Lett.* **2018**, *9*, 5474−5480.

https://dx.doi.org/10.1021/jacs.0c09132